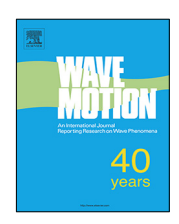


Contents lists available at ScienceDirect

Wave Motion

journal homepage: www.elsevier.com/locate/wamot



Tailoring reflected and diffracted wave fields from tessellated acoustic arrays by origami folding



Chengzhe Zou, Ryan L. Harne*

Department of Mechanical and Aerospace Engineering, The Ohio State University, Columbus, OH 43210, USA

ARTICLE INFO

Article history:
Received 27 July 2018
Received in revised form 20 February 2019
Accepted 4 March 2019
Available online 8 March 2019

ABSTRACT

Recently the physical reconfigurations of origami-inspired acoustic arrays have been leveraged for adaptive guidance of acoustic wave energy. The spatial translations and rotations of transducer elements in tessellated arrays may tailor how reflected and diffracted waves contribute to the total acoustic pressure at the field point. To date such wave phenomena have not been illuminated, which inhibits understanding on how to best leverage the concept for highly reconfigurable arrays. Here, the reflection and diffraction phenomena induced from a Miura-ori based acoustic array are examined, wherein such wave fields superpose with directly radiated waves to yield the total acoustic response at receiving locations. As tessellated arrays take on highly folded configurations, reflected waves are shown to greatly contribute to the acoustic field at points normal to the plane of the unfolded array, whereas diffracted waves primarily govern the acoustic pressure for locations at nearly grazing angles of incidence to the unfolded array plane. Supported by experimental validation, the modeling methods established here can be extended to arbitrary wave-radiating architectures and may inspire investigations for other physical domains where reconfigurable array concepts are of great interest.

© 2019 Elsevier B.V. All rights reserved.

1. Introduction

The emergence of origami science has inspired innovative materials and structures to control waves in diverse physical fields. The properties of such systems are governed by the geometric shape and consequently the reconfigurations of origami architecture adapt functionality. For example, origami-based platforms are leveraged to tune the properties of waveguides [1–3], radio frequency antennas [4–7], and optical imaging devices [8–10], among others.

Acoustic arrays are another embodiment of wave guiding systems in which energy delivery to space may be tailored through the folding-induced redistribution of acoustic transducer elements [11]. In such a concept, the tessellated facets of origami structures act as baffled oscillating pistons to radiate acoustic waves, which is exemplified by the acoustic array built upon the Miura-ori architecture shown in Fig. 1(a). With the shape change of the tessellation, the transducers are redistributed and the acoustic interference effects are tailored to control the acoustic pressure field. Such adaptive wave guiding is comparable to the objective of digital control of spatially fixed transducer elements in acoustic arrays [12]. Yet, the physical reconfiguration of transducer elements by an origami-inspired approach to wave control has several advantages over the digital counterparts, including straightforward implementation and unique portability [11–14]. In consequence, the acoustic wave guiding enabled by reconfigurable tessellated arrays suggests promising potential to

E-mail address: harne.3@osu.edu (R.L. Harne).

^{*} Corresponding author.

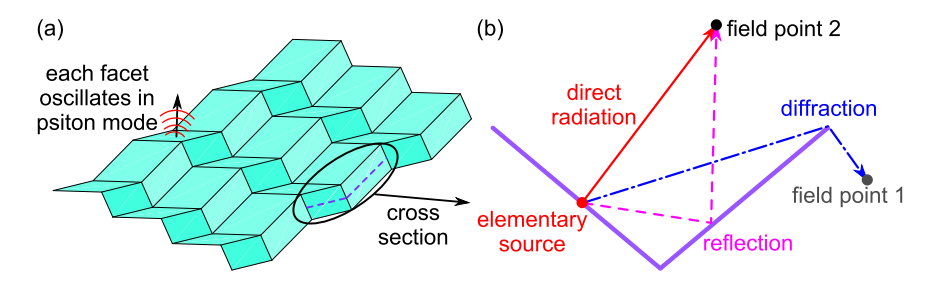


Fig. 1. (a) Miura-ori tessellation with oscillating facets to radiate acoustic waves. (b) Two-dimensional illustration of reflection and diffraction that may exist in reconfigurable tessellated acoustic array.

advance applications as diverse as underwater monitoring [15], ultrasonic surgical treatments [16], and non-destructive evaluation [17], for which digital methods of wave control are challenged by real-time implementation and/or system compactness.

Due to such advantages, an analytical framework has been composed to investigate the properties of reconfigurable tessellated acoustic arrays [11,13]. To date, these models evaluate Rayleigh's integral over the tessellated surfaces to characterize the directly radiated acoustic pressure. Yet, reconfigurations of wave-radiating tessellations may cause reflected and diffracted acoustic fields that are not accounted for via Rayleigh's integral. In fact, reflection and diffraction may contribute notably to the total acoustic field, as illustrated by the cross-section of two adjacent facets in a Miura-ori transducer element in Fig. 1(b). Diffraction is the only means by which the elementary source on the transducer surface delivers acoustic energy to field point 1 because the direct radiation path (line-of-sight) is blocked by the adjacent folded facet. This indicates that diffraction is paramount to acoustic fields that are located in acoustic shadows. In fact, even for the field point 2 that can be reached by direct radiation, predictions of acoustic fields by Rayleigh's integral deviate from numerical results [13]. These deviations mainly derive from the reflected waves caused by adjacent radiating surfaces that face each other. The influences of the reflected field are intense if the distances among facets are within a few wavelengths [18], which is common for the tessellated acoustic arrays considered to date [12]. Since reflection and diffraction are not taken into account in previous studies [11,13], great insights remain to be uncovered on the overall acoustic fields emitted from reconfigurable tessellated acoustic arrays.

In order to achieve comprehensive understanding of the wave fields, analytical formulations need to be composed to uncover the influences of reflection and diffraction in relation to direct radiation. Indeed, reflection and diffraction of acoustic waves are widely investigated. As surveyed in Ref. [19], reflection is extensively characterized in architectural acoustics. In these contexts, reflection is modeled using assumptions of reflecting surfaces that are significantly larger than the acoustic wavelength [20–24]. Such assumption is not appropriate for tessellated arrays because the sizes of the reflecting facets are often on the order of the acoustic wavelength [12]. Diffraction is also widely modeled in problems involving sonic barriers, as reviewed in Ref. [25]. Numerous solutions of diffracted fields are available for scenarios considering plane incident waves or semi-infinite barriers [26–30]. Yet, neither attribute is exhibited in foldable arrays since the waves remain spherical along the barrier edges where diffraction occurs and the barriers are of finite extent. It is evident that the reflected and diffracted acoustic fields emitted from reconfigurable tessellated arrays present unique physics compared to past investigations. Addressing these new problems requires an inclusive framework to model the acoustic field culminating all together from direct radiation, reflection, and diffraction.

This research aims to elucidate how reflection and diffraction contribute to the total acoustic fields radiated from reconfigurable tessellated acoustic arrays. In this work, the Miura-ori tessellation is investigated due to the broad relevance for wave guiding applications [2,11,31]. Here, analytical models are developed for a Miura-ori-based transducer element and for an array assembled from such elements. The efficacy of the theoretical approach to account for reflection and diffraction is demonstrated through comparisons to experimental and numerical outcomes. The influences of reflection and diffraction on the total radiated acoustic field are characterized and shown to dramatically govern the total acoustic characteristics for folded element and array. A summary of the key contributions and discoveries from this research concludes the report.

2. Total acoustic field emitted from a Miura-ori transducer element

In this section, an analytical framework is developed to predict the far field acoustic pressure delivered from a transducer element shaped in the Miura-ori folding pattern. Throughout this work, the tessellated facets are assumed to be rigid and the creases are considered as ideal kinematic hinges. For acoustic modeling, far field conditions are met for the field point receiving the acoustic waves emitted from the transducer elements. In the derivation, acoustic pressure and particle velocity are time-harmonic, while the time dependent term $e^{i\omega t}$ is omitted for brevity.

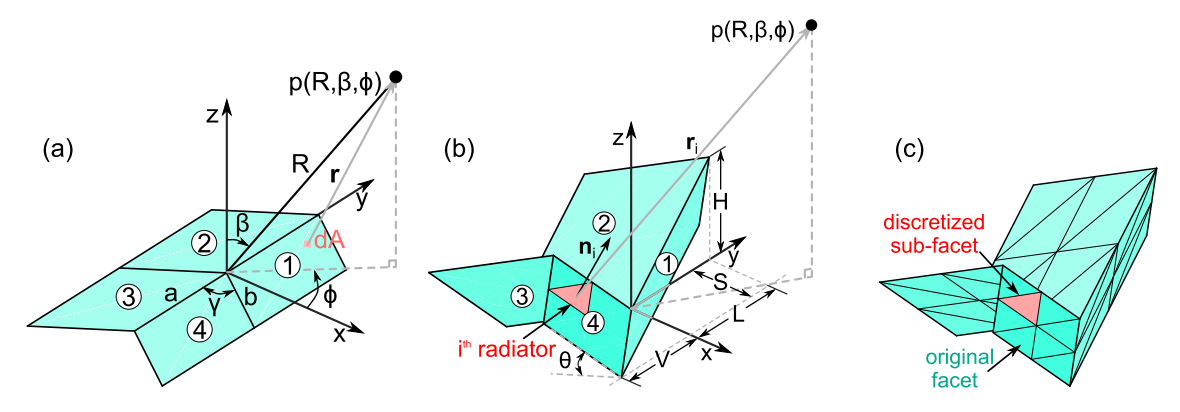


Fig. 2. (a) Geometric and acoustic modeling notations of the unfolded Miura-ori element. (b) Geometric shape of folded Miura-ori element and geometric notation of spatial extents. (c) Discretization of original facets into sub-facets.

2.1. Analytical model formulation for a Miura-ori transducer element

2.1.1. Direct radiation from oscillating facets

The unfolded geometry of a Miura-ori transducer element is shown in Fig. 2(a). The topology is determined by edge lengths a and b and edge angle γ . The tessellated facets are assumed to be rigid pistons that are individually baffled and oscillate in an axis normal to the plane of the facet surface. The spherical coordinate system of radial distance R, elevation angle β , and azimuth angle ϕ is used to define the location of the far field point, as shown in Fig. 2(a). By Rayleigh's integral, the acoustic pressure radiated to the field point from the oscillating facets of Miura-ori element is

$$\overline{p}(R,\beta,\phi) = j \frac{\rho_0 \omega u_0}{2\pi} \int_A \frac{e^{-jk|\mathbf{r}|}}{|\mathbf{r}|} dA \tag{1}$$

The \bar{p} is the acoustic pressure from the Miura-ori element; ρ_0 is the medium density; ω is the angular oscillating frequency; u_0 is the amplitude of the normal velocity over radiating surface; $k = \omega/c_0$ is the acoustic wavenumber with sound speed c_0 ; and \mathbf{r} is the vector from the differential area dA to the field point.

For the folded Miura-ori element in Fig. 2(b), the dihedral angle θ between facet 4 and x-y plane is introduced to specify the influence of folding. The folded shape can be described by the spatial extents H, S, L, and V that are derived in Ref. [32] and provided in Appendix A of this work.

As described in Section 1, the folded facets may intercept the direct line-of-sight path between the differential radiating area and the field point. Yet, the line-of-sight may vary considerably from one differential area dA to another, even for the same field point. To address this issue, the radiating surfaces are discretized into sub-facets. Then, each sub-facet is modeled as a point source [33]. Such discretization is exemplified in Fig. 2(c). The discretization shown in Fig. 2(c) is for illustration purpose only. Since the definition of point source is dependent on the acoustic wavelength, the discretization employed in computation throughout this work is refined to guarantee that the discretized sub-facets are accurately modeled as point sources [33,34].

For the ith point source, the directly radiated acoustic pressure at the field point is

$$\overline{p}_{rad}^{i} = j \frac{\rho_0 \omega u_0}{2\pi} \frac{e^{-jk|\mathbf{r}_i|}}{|\mathbf{r}_i|} A_i \tag{2}$$

The superscript i indicates the contribution from the ith source, A_i is the area of the ith source, and \mathbf{r}_i is the vector from the geometric center of the ith source to the field point.

For the line-of-sight to exist between the source and field point, the field point must be above the baffled plane wherein the *i*th radiator lays [35]

$$\mathbf{r}_i \cdot \mathbf{n}_i > 0 \tag{3a}$$

The \mathbf{n}_i is the 'upward' normal vector of the *i*th source that points toward the acoustic field occupying positive values of the *z* axis, as shown in Fig. 2(b).

The barrier effect induced by folded facets depends on the location of field point. Taking the field point in the octant of (+x, +y, +z) in Fig. 2(b) for instance, only facet 1 is able to block the acoustic waves that are radiated into this space while other facets do not act as barriers. For direct radiation, the intersection of \mathbf{r}_i and the plane that the barrier lies in should be outside the spatial range of the barrier. To guarantee the line-of-sight between the source and the receiver, the following inequalities must be satisfied

$$x_{\text{int}1} < 0 \text{ or } x_{\text{int}1} > S \text{ or } y_{\text{int}1} < -V \text{ or } y_{\text{int}1} > L \text{ or } z_{\text{int}1} < 0 \text{ or } z_{\text{int}1} > H$$
 (3b)

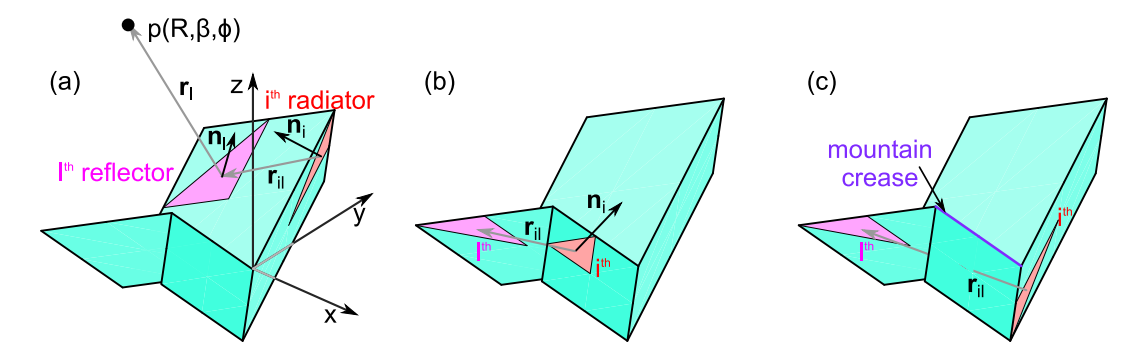


Fig. 3. (a) Analytical model notation to consider the reflection between facets in Miura-ori element. (b) The *l*th reflector is beneath the baffle plane of the *i*th radiator. (c) Line-of-sight between the *i*th and *l*th sub-facets is intercepted by the facet includes mountain crease.

The $(x_{\text{int1}}, y_{\text{int1}}, z_{\text{int1}})$ refers to the location of the intersection in the coordinate system defined in Fig. 2(b), and the detailed derivation is given in Appendix B.

To account for the direct radiation from the *i*th radiator to the field point, Eq. (3) must be satisfied, otherwise Eq. (2) does not contribute to the directly radiated acoustic field.

2.1.2. Reflections among the facets of a Miura-ori transducer element

The influence of reflection is considered by modeling the first reflection between a radiating facet and the neighboring facets. The first reflection refers to the acoustic waves that are only reflected once before arriving at the field point. For spherical waves, the acoustic pressure amplitude varies in inverse proportion with the distance to the source. Consequently, the first reflection is anticipated to contribute more significantly to the field point acoustic pressure than reverberations that take multiple reflected paths to the field point. Since the facets are assumed to be rigid, the normal particle velocity due to incident waves vanishes on reflective surfaces [18]. In order to satisfy this boundary condition, the normal velocity over reflecting surfaces cancels the normal velocity caused by incident waves from adjacent radiating sub-facets.

Using the notation in Fig. 3(a), the acoustic pressure on the *l*th reflecting sub-facet due to the radiation from the *i*th point source on an adjacent facet is

$$p^{i \to l} = j \frac{\rho_0 \omega u_0}{2\pi} \frac{e^{-jk|\mathbf{r}_{il}|}}{|\mathbf{r}_{il}|} A_i \tag{4}$$

The \mathbf{r}_{il} is the vector from the geometric center of the *i*th radiator to that of the *l*th sub-facet.

Considering that the wave arriving at the reflecting sub-facet is spherical, the normal particle velocity on the surface of the *l*th reflector to cancel the normal velocity caused by $p^{i\rightarrow l}$ is

$$u_{unit}^{i \to l} = \left[1 - \frac{j}{k |\mathbf{r}_{il}|}\right] \frac{p^{i \to l}}{\rho_0 c} \frac{|\mathbf{r}_{il} \cdot \mathbf{n}_l|}{|\mathbf{r}_{il}| |\mathbf{n}_l|}$$
(5)

where $u_{unit}^{i \to l}$ points toward the positive direction of \mathbf{n}_l .

Utilizing Eq. (5) requires that the *i*th radiator is able to project acoustic pressure onto the *l*th reflector. Three geometric conditions must be satisfied to guarantee the line-of-sight between these two sub-facets.

- I. The *l*th reflective sub-facet is not on the same facet with the *i*th source.
- II. The *l*th reflecting sub-facet is above the baffle plane of the *i*th source. Fig. 3(b) shows one counter-example.
- III. The line-of-sight is not intercepted by the facets that include a mountain crease, provided that they are distributed on both sides of y-z plane. The sub-facets shown in Fig. 3(c) satisfy conditions I and II, but the direct path between them is not available due to the mountain crease.

To satisfy conditions I and II, Eqs. (6a) and (6b) need be met, respectively

$$\frac{\mathbf{n}_i \cdot \mathbf{n}_l}{|\mathbf{n}_i| \cdot |\mathbf{n}_l|} \neq 1 \tag{6a}$$

$$\mathbf{r}_{il} \cdot \mathbf{n}_i > 0 \tag{6b}$$

For condition III, the intersection of \mathbf{r}_{il} and the y-z plane that the mountain crease lies in is first identified. Then, to satisfy condition III, this intersection should be above the mountain crease for line-of-sight

$$z_{\rm int2} > -\frac{H}{L} y_{\rm int2} \tag{6c}$$

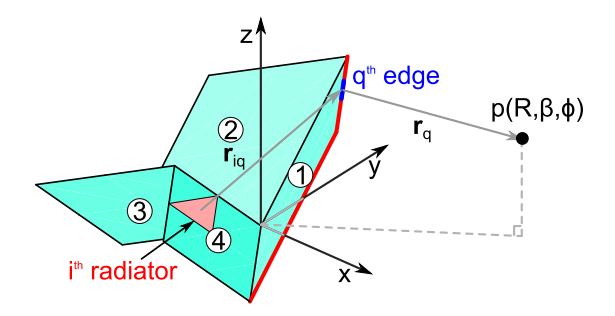


Fig. 4. Analytical model notation to consider the diffraction from the edges of Miura-ori element.

The $(x_{\text{int2}}, y_{\text{int2}}, z_{\text{int2}})$ is the location of the intersection of \mathbf{r}_{il} and the y-z plane, and its expression is provided in Appendix B. The $z(y) = -\frac{H}{L}y$ is the function of the mountain crease in y-z plane. Then the normal velocity on the lth reflector due to radiation from other sub-facets is

$$u_{unit}^{l} = \sum_{i=1}^{M} \left[1 - \frac{j}{k |\mathbf{r}_{il}|} \right] \frac{p^{i \to l}}{\rho_0 c} \frac{|\mathbf{r}_{il} \cdot \mathbf{n}_{l}|}{|\mathbf{r}_{il}| |\mathbf{n}_{l}|}$$

$$(7)$$

Therefore the *l*th reflective sub-facet is transformed as a radiator with normal velocity obtained from Eq. (7). In order to account for the reflected waves, the field point must be in the line-of-sight of the reflective sub-facet, analogous to the geometric criteria in Eq. (3) for direct radiation.

The acoustic pressure at the field point due to the reflection of the incident waves on the Ith sub-facet is

$$\overline{p}_{\eta l}^{l} = j \frac{\rho_0 \omega u_{unit}^{l}}{2\pi} \frac{e^{-jk|\mathbf{r}_l|}}{|\mathbf{r}_l|} A_l \tag{8}$$

2.1.3. Diffraction from the edges of a Miura-ori transducer element

In this work, the acoustic waves diffracted by the tessellated facets of a Miura-ori element are modeled as waves radiated from secondary sources on the edges of these facets. Based on the strategy of the minimum diffraction path [36], the fundamental solution of the sound diffracted by a barrier edge is

$$p_{dif} = \frac{B}{d}e^{-jkd}e^{j\varphi} \tag{9}$$

The B/d is the amplitude of the diffracted acoustic waves, d is the length of the diffraction path from the source to the edge and then to the field point, and φ is the phase variation due to the barrier.

The phase variation φ is a function of barrier configuration [27]. It approaches an asymptotic limit of $\pi/4$ at high frequencies for field points that are in the far field of the edge location [28,36]. The asymptotic limit is applicable for the problems of interest here. In other words, acoustic sources are close to the edges associated with diffracted waves while the receiving point is in the far field respecting the edge locations. Therefore the constant of $\varphi = \pi/4$ is utilized in this work with Eq. (9).

To utilize the fundamental solution in Eq. (9), the source and the edge that result in the diffracted wave field are first identified. The edges that emit diffracted waves are related to the location of the field point respecting the facet source point, which is the same distinction of barrier effects described in Section 2.1.1. An example considering a field point in the octant (+x, +y, +z) is given to illustrate the computation of diffracted waves. For field points in the domain of (+x, +y, +z), the diffracted waves are emitted from the edges of facet 1 since this facet blocks the acoustic waves radiated into this region. Nevertheless, only the two red edges of the facet 1 shown in Fig. 4 diffract waves since the other two edges of facet 1 are valley creases.

Here the edges that lead to diffraction are discretized. A segment of such a discretized edge is shown in Fig. 4 as the qth edge segment. For the ith radiating source on one facet, the acoustic pressure at the field point associated with the diffracted waves from the edges of another facet is

$$\bar{p}_{dif}^{i} = \sum_{q=1}^{W} j \frac{\rho_0 \omega u_0}{2\pi} \frac{A_i}{|\mathbf{r}_{iq}| + |\mathbf{r}_q|} e^{-jk(|\mathbf{r}_{iq}| + |\mathbf{r}_q|)} e^{j\frac{\pi}{4}} \frac{L_q}{L_{edge}}$$

$$\tag{10}$$

The W is the number of discretized edge segments; L_q is the length of the qth segment; L_{edge} is the total length of the edge for diffraction.

Being similar to reflection, not all point sources have lines-of-sight with the qth edge. Consequently three geometric conditions must be satisfied to count the diffraction in Eq. (10) by replacing the center of the lth reflector in Eq. (6) with the center of the qth edge segment.

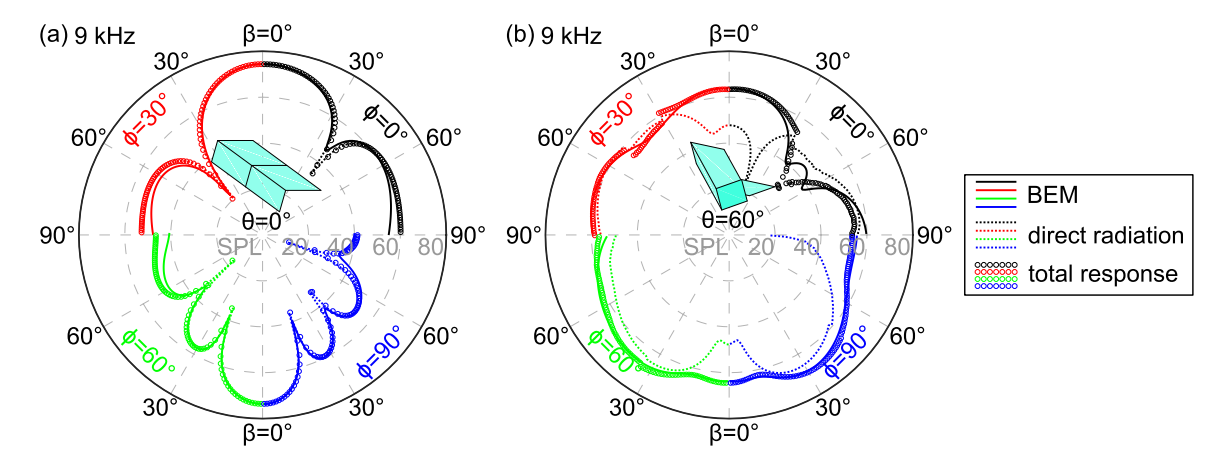


Fig. 5. SPL of Miura-ori element as a function of elevation angle β of field point. Each plot compares BEM results, analytical predictions of direct radiation, and analytical predictions of total response (direct radiation, reflection, and diffraction). Different quadrants/colors correspond to azimuth angles $\phi = 0^{\circ}$, 30° , 60° , and 90° , respectively. Folding angles θ are 0° (a) and 60° (b). Driving frequency is 9 kHz and radial distance is 5 m for both plots . (For interpretation of the references to color in this figure legend, the reader is referred to the web version of this article.)

2.1.4. Total acoustic pressure received at the field point from a Miura-ori transducer element

The total acoustic pressure at the far field point is then the sum of contributions from direct radiation, reflection, and diffraction.

$$\overline{p} = \sum_{i=1}^{M} \left(\overline{p}_{rad}^{i} + \overline{p}_{rfl}^{i} + \overline{p}_{dif}^{i} \right) \tag{11}$$

The *M* is the number of discretized sub-facets in the Miura-ori transducer element.

To quantify the directive acoustic response at the field point, the sound pressure level (SPL) is computed.

$$SPL = 20 \log 10 \left[\frac{p_{\rm rms}}{p_{\rm ref}} \right] \tag{12}$$

The subscript rms is the root mean square value of the acoustic pressure, and the reference pressure is $p_{\rm ref} = 20~\mu \text{Pa}$.

2.2. Contributions of diffracted and reflected waves from a reconfigurable Miura-ori transducer element

Rayleigh's integral can be considered to be a special case of Kirchhoff–Helmholtz (K–H) integral equation for the situation that the vibrating surfaces lie in a single infinite baffle plane [34]. The K–H equation is an effective transformation of the acoustic wave equation so that solutions to the K–H equation for folded tessellated acoustic arrays include reflected and diffracted waves. Since the boundary element method (BEM) solves the K–H equation [37], BEM simulations are used to verify the analysis in this work [38,39]. Throughout analysis and BEM, air is utilized as the fluid medium with $\rho_0 = 1.104 \text{ kg/m}^3$ and $c_0 = 343 \text{ m/s}$.

Fig. 5 presents a comparison of BEM and analytical results for acoustic pressure at the far field point delivered from a Miura-ori transducer element. The total acoustic pressure received at the field point is computed by BEM and shown by solid curves. Analytical predictions of the direct radiation determined by Rayleigh's integral are shown by dotted curves, whereas analytical predictions that include direct radiation, reflected waves, and diffracted waves are shown by circles. In each polar plot, SPL is presented as a function of elevation angle $\beta \in [0^{\circ}, 90^{\circ}]$ using different quadrants and colors for azimuth angles $\phi = 0^{\circ}$, 30° , 60° , and 90° . Such characterizations are referred to as the *beam pattern* of the element, which is a metric of the elevation and azimuthal directionalities of the acoustic waves delivered to the far field. The facet dimensions of the Miura-ori element are a = 60 mm, b = 40 mm, and $\gamma = 50^{\circ}$. The unfolded configuration $\theta = 0^{\circ}$ that should hypothetically exhibit only direct radiation is shown in Fig. 5(a), while Fig. 5(b) presents results for a highly folded state of $\theta = 60^{\circ}$ that introduces reflection and diffraction to the directly radiated field. For the folded case in Fig. 5(b), the geometric characteristics to realize acoustic baffle (or shadow) conditions in Eq. (3a) lead to discontinuities in the analytical results in Fig. 5. This is because the discretized sub-facets on one facet may lose the lines-of-sight at the same time when the field point just moves beneath the baffle plane. The driving frequency and radial distance are 9 kHz and 5 m, respectively, for both plots. The largest dimension of the discretized sub-facet is 3.75 mm, which indicates that there are at least 10.01 sub-facets per wavelength at 9 kHz.

For the unfolded state in Fig. 5(a), the analytical predictions of direct radiation and total response are nearly the same because there are no contributions from reflection or diffraction to the field when the radiating surfaces are perfectly flat. From Fig. 5(a), it is observed that the direct radiation predictions agree well with the BEM results. The magnitudes and

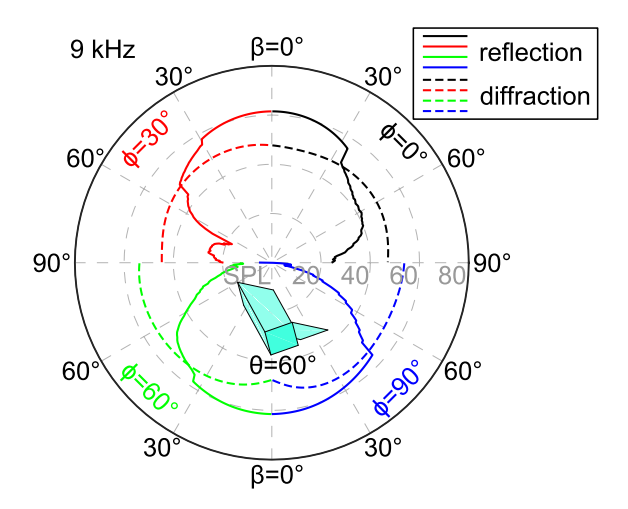


Fig. 6. SPL of Miura-ori element as a function of elevation angle β of field point. The contributions due to reflection and diffraction are respectively plotted. Different quadrants/colors correspond to azimuth angles $\phi=0^\circ$, 30° , 60° , and 90° , respectively. Folding angle θ is 60° , driving frequency is 9 kHz, and radial distance is 5 m . (For interpretation of the references to color in this figure legend, the reader is referred to the web version of this article.)

breadths of main lobe and sidelobes, the numbers and angular locations of SPL nodes, and other characteristics are all quantitatively reconstructed by analysis. Here node refers to the field point of local minimum SPL. The small deviations between analysis and BEM for the cases shown in Fig. 5(a) are from the numerical errors that result from the different discretizations of the domains present between BEM and analytical computations.

Nevertheless, such agreement between direct radiation and BEM is significantly lessened in Fig. 5(b) where $\theta=60^\circ$. For the folded Miura-ori element in Fig. 5(b), it is observed that at $\beta=0^\circ$, also termed *broadside*, the SPL in BEM is 64 dB while the analytical prediction of direct radiation is 48 dB. In the azimuth plane of $\phi=90^\circ$ at the *endfire* location $\beta=90^\circ$, the directly radiated SPL is 40 dB lower than the BEM result. Such discrepancies and others that are evident in Fig. 5(b) indicate that only considering the direct radiation from the folded element is inadequate to characterize the acoustic field. In fact, the total acoustic pressure predicted by the analytical formulation devised here enhances the agreement to BEM results substantially. By accounting for the influences of reflection and diffraction, the total response in Fig. 5(b) exemplifies that quantitative agreement is achieved between analysis and BEM at broadside and endfire sides. For other angular locations, the total responses are also in good agreement despite minor discrepancies. These deviations mainly arise from the multiple reflections among facets that are neglected in the present analysis and the fact that the assumptions employed to model diffraction may not be comprehensively satisfied. On the other hand, the good agreement between the total acoustic pressure response predicted analytically and the BEM simulations is also observed in Supplementary Fig. 1 through considerations of other frequencies and wavelengths of acoustic wave radiation from the tessellated transducer element. Yet, how the distinct wave phenomena contribute to the acoustic field remains to be uncovered.

To bring the underlying physics to light, the SPL values associated with reflection and diffraction that contribute to the total response in Fig. 5(b) are plotted in Fig. 6. Due to the considerations of Eq. (3a), there are discontinuities in the prediction of reflection since it contributions from reflections are also influenced by the acoustic baffle conditions. The reflection contributions are shown as solid curves, whereas the diffracted wave SPL values are shown as dashed curves, using the same polar and azimuthal ϕ plotting conventions as in Fig. 5. From Fig. 6, it is observed that reflection contributes more than 60 dB to the broadside, which explains why the total response at $\beta=0^{\circ}$ is increased significantly from direct radiation in Fig. 5(b). In fact, the SPL at the angular regions around broadside are all increased due to reflection. As shown in Fig. 6, the majority of reflected acoustic energy is concentrated for $\beta \in [0^{\circ}, 30^{\circ}]$. Here the upper limit approximately coincides with the difference between 90° and the folding angle $\theta=60^{\circ}$. This coincidence can be physically explained by recalling the definition of folding angle in Fig. 2(b): the reflected acoustic waves are constrained within the space closed by folded facets. Although the dimensions of the folded facets are insignificant compared with the radial distance, the reflections among them are still influential contributions to the total far field acoustic pressure because the reflections occur in the near fields of the sources themselves.

Compared with reflection, diffraction plays a more dominant role for elevation angles closer to the endfire location $\beta=90^\circ$ than at broadside $\beta=0^\circ$. Taking the endfire side at azimuth angle $\phi=90^\circ$ for instance, the total response SPL of 56 dB is entirely due to diffraction, which is seen by comparing Fig. 5(b) and Fig. 6. The dominance of diffraction is because neither directly radiated nor reflected waves reach an endfire location when the field point azimuth is $\phi=90^\circ$. Such trend is also observed for $\phi=60^\circ$, but it is not evident for $\phi=0^\circ$ and 30° because the SPL of the directly radiated acoustic wave is comparable to the total response SPL near the endfire positions in Fig. 5(b). The variation of diffraction with azimuth angles is due to the locations and orientations of the relevant facet acoustic barriers. The heights of the barriers for $\phi=0^\circ$

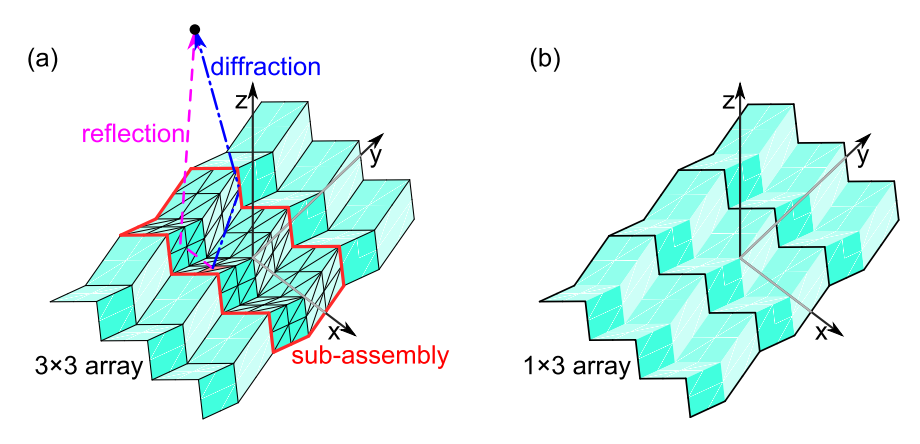


Fig. 7. (a) Illustration of reflection and diffraction that may occur between neighboring elements in Miura-ori array (3 \times 3). The red lines outline the sub-assembly whose surface is discretized for acoustic pressure prediction. (b) Line array (1 \times 3) composed from the sub-assemblies in (a), which is acoustically equivalent with the Miura-ori array (3 \times 3) in (a)

and 30° are not as great as those in the other two azimuth locations. Consequently, the relative significance of diffraction to the total response is decreased. Additional exemplary cases of these trends are revealed through the Supplementary Fig. 2 and complement the insights gained here. The analytical framework developed for the element in this section paves the way for the following study to model the reflection and diffraction from the array assembled from such elements.

3. Total acoustic field emitted from an array of Miura-ori transducer elements

3.1. Analytical model formulation for a Miura-ori array

An acoustic array assembled from Miura-ori transducer elements is shown in Fig. 7(a). The numbers of Miura-ori elements in the x and y axes are respectively M_x and M_y . Therefore the size of the Miura-ori array in Fig. 7(a) is 3 \times 3. The beam pattern of an acoustic array is usually the product of the beam pattern of array element and the array factor [40]. Yet, one requirement to use the product theorem is that the array elements are mutually independent. This assumption is not satisfied for tessellated arrays because reflection and diffraction exist among neighboring elements, as shown in Fig. 7(a).

By examining the Miura-ori array in Fig. 7(a), it is seen that the mountain creases between Miura-ori elements in the y axis prevent mutual reflections among transducer elements that are arrayed in the x axis. On the other hand, reflected waves exist among neighboring elements in the x axis as shown in Fig. 7(a). Consequently it is assumed that Miura-ori elements are independent when assembled in the y axis. Based on this assumption, the Miura-ori elements in the x axis are assembled and the perimeter of such a sub-assembly is illustrated by the red outline in Fig. 7(a). As a result, the original two-dimensional array of Miura-ori elements is reassembled into a line array of the sub-assemblies, as exemplified in Fig. 7(b). Then the one-dimensional array factor in the y axis is employed to characterize the influences of the total acoustic pressure at the field point due to the assembly of 1×3 sub-assemblies.

The beam pattern of the sub-assembly includes contributions from direct radiation, reflection, and diffraction. Directly radiated waves from the Miura-ori elements in the sub-assembly are not influenced by neighboring facets. As a result, the product theorem in the x axis is utilized to obtain the total directly radiated acoustic pressure from the sub-assembly. The D_x is the array factor in the x axis.

$$\hat{p}_{rad} = \bar{p}_{rad} D_x M_x \tag{13}$$

$$D_{x} = \frac{\sin[M_{x}kS\sin\beta\cos\phi]}{M_{x}\sin[kS\sin\beta\cos\phi]}$$
(14)

The mutual reflection between nearest neighboring Miura-ori elements is accounted for, which is greater than the reflections from more distant elements due to shorter paths of first reflection. For the sub-assembly illustrated in Fig. 7(a), there are three different cases to consider. For the leftmost element in the x axis, reflection among the local facets as well as reflection from the right-neighboring element are manifest. For the rightmost element in the x axis, reflection among the local facets and reflection from the left-neighboring element are present. These cases contrast to the middle element that experiences 'self-reflection' as well as reflections resulting from the left- and right-neighboring elements.

Then the acoustic pressure due to reflections among the elements in the sub-assembly is

$$\hat{p}_{rfl} = j \frac{\rho_0 \omega}{2\pi} A_i \sum_{i=1}^{MM_x} \frac{u^i e^{-jk|\mathbf{r}_i|}}{|\mathbf{r}_i|} \tag{15}$$

The u^i is the normal velocity associated with reflection, and u^i is a function of the location of the Miura-ori element in the sub-assembly.

$$u^{i} = \begin{cases} u^{i}_{unit} + u^{i}_{r \to l} & 1 \le i \le M \\ u^{i}_{unit} + u^{i}_{r \to l} + u^{i}_{l \to r} & otherwise \\ u^{i}_{unit} + u^{i}_{l \to r} & (M_{x} - 1)M + 1 \le i \le M_{x}M \end{cases}$$
(16)

The numbering of discretized reflective sub-facets starts from the left in the assembly. The $u^i_{r\to l}$ and $u^i_{l\to r}$ refer to the normal velocity on the surface of the ith reflector due to its right and left neighbors, respectively. $u^i_{r\to l}$ and $u^i_{l\to r}$ are acquired in comparable ways with u^i_{unit} .

The computation of the diffracted fields from the sub-assembly of Miura-ori elements is undertaken in ways similar to those for reflection that are described above. For the *i*th radiator in the sub-assembly, the acoustic pressure delivered to the far field point due to diffracted waves is

$$\hat{p}_{dif}^{i} = \begin{cases} \bar{p}_{dif}^{i} + \bar{p}_{dif(l \to r)}^{i} & 1 \le i \le M \\ \bar{p}_{dif}^{i} + \bar{p}_{dif(l \to r)}^{i} + \bar{p}_{dif(r \to l)}^{i} & otherwise \\ \bar{p}_{dif}^{i} + \bar{p}_{dif(r \to l)}^{i} & (M_{x} - 1)M + 1 \le i \le M_{x}M \end{cases}$$
(17)

The $\bar{p}^i_{dif(r \to l)}$ and $\bar{p}^i_{dif(l \to r)}$ refer to the diffracted sound from the *i*th radiator due to edges of its right and left neighbors, respectively, and they are obtained similarly with \bar{p}^i_{dif} .

Then the total contribution from diffraction in the sub-assembly to the field point is

$$\hat{p}_{dif} = \sum_{i=1}^{MM_x} \hat{p}_{dif}^i \tag{18}$$

With Eqs. (13), (15), and (18), the total acoustic pressure at the field point delivered from the sub-assembly of Miura-ori transducer elements in the x axis is

$$\hat{p} = \hat{p}_{rad} + \hat{p}_{rfl} + \hat{p}_{dif} \tag{19}$$

The array factor in the y axis is

$$D_{y} = \frac{\sin\left[M_{y}kL\sin\beta\sin\phi\right]}{M_{y}\sin\left[kL\sin\beta\sin\phi\right]} \tag{20}$$

With the beam pattern of the sub-assembly and the array factor known, the total acoustic pressure at the field point due to radiation from the Miura-ori acoustic array is

$$p = \hat{p}D_{\nu}M_{\nu} \tag{21}$$

3.2. Influences of reflection and diffraction in the acoustic field from a Miura-ori acoustic array

The far field SPL emitted from a Miura-ori array is presented in Fig. 8. The array size is 3×2 and the geometry of the Miura-ori elements and its discretization are the same as those studied in Figs. 5 and 6. The folding angle is $\theta = 60^{\circ}$ and the radial distance is 5 m. The BEM outcomes and analytical results of the total acoustic pressure response are compared in Fig. 8(a) and (b) for 6 kHz and 11 kHz, respectively. Both the color and radial distance from the origin indicate the magnitude of the SPL at that position. The ranges of elevation and azimuth angles are $[0^{\circ}, 90^{\circ}]$. For ease of comparison, the analysis (left) and BEM (right) results are presented in a mirrored way.

Considering the Miura-ori array driven at 6 kHz in Fig. 8(a), the SPL values are nearly symmetric between the left and right portions of the plot, which indicates the analysis achieves good agreement with BEM. In addition, both results identify that the maximum SPL occurs for $\beta \epsilon$ [20°, 60°] and $\phi \epsilon$ [45°, 90°]. This is different from flat acoustic arrays wherein the most constructive interference is always at broadside. The atypical location of major lobe is because the acoustic energy that is delivered to broadside when the array is unfolded is subsequently redirected by folding. This suggests that the location of the maximum SPL may be tuned by the reconfiguration of the tessellated facets. Yet, such tuning depends on the relative dimensions comparing the acoustic wavelength to the geometric dimensions. For high frequencies such as 11 kHz in Fig. 8(b), there are multiple wavelengths spanning the largest facet dimension. As such, the wave radiation from a single facet is highly directive, so that the SPL cannot be intuitively tuned by folding due to intricate interference effects. On the other hand, if the array dimension is smaller than a wavelength, the array radiates acoustic waves like a monopole. In this case, the location of maximum SPL may also not be tuned since folding an array that radiates sound like a monopole does not substantially change the monopole-like wave emission. Only for the mid-range frequencies, such 5 kHz in Fig. 8(a) used in this work, for which the wavelength is comparable to the largest facet dimension will folding actions considerably influence the location of maximum SPL.

Greater insights are extracted from two-dimensional slices of the three-dimensional surface plots. The beam patterns in the azimuth planes of $\phi = 0^{\circ}$, 30° , 60° , and 90° of Fig. 8(a) and (b) are presented in Fig. 8(c) and (d), respectively.

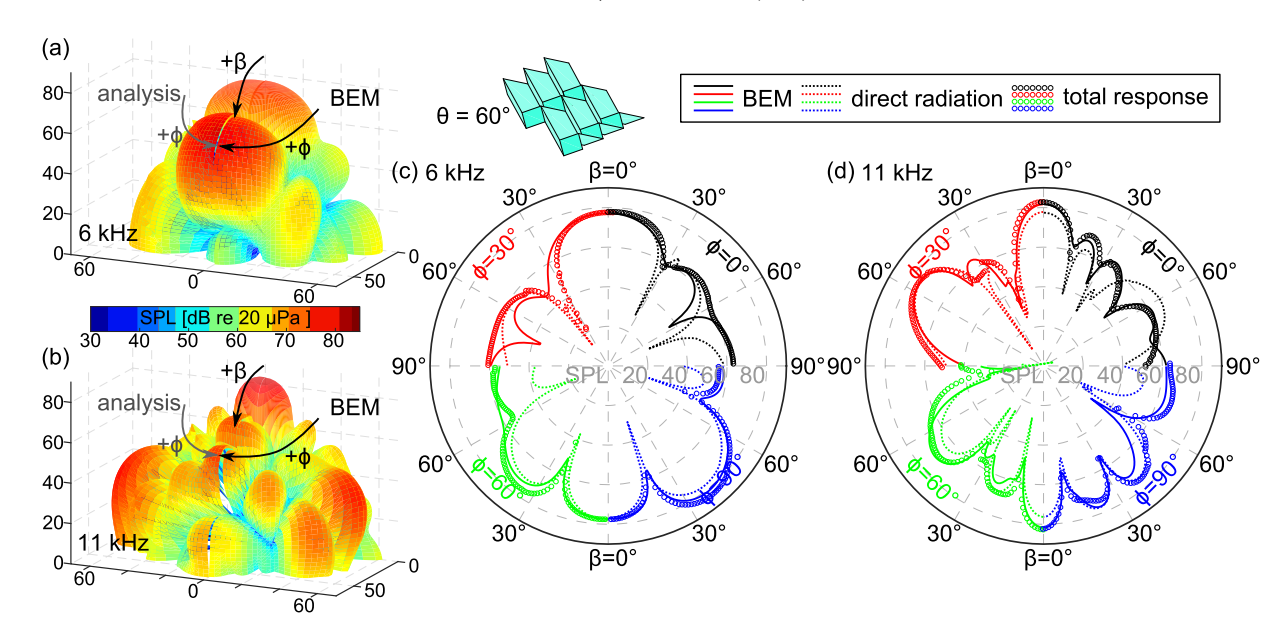


Fig. 8. (a, b) SPL of Miura-ori array (3 × 2) as a function of elevation angle β and azimuth angle ϕ of field point. Each plot compares the analysis (left) and BEM (right) results. Both color and radial distance from the origin indicate the magnitude of the SPL. (c, d) SPL of Miura-ori array (3 × 2) as a function of elevation angle β of field point. Each plot compares BEM results, analytical predictions of direct radiation, and analytical predictions of total response (direct radiation, reflection, and diffraction). Different quadrants/colors correspond to azimuth angles ϕ = 0°, 30°, 60°, and 90°, respectively. Folding angle θ is 60° for all plots, and driving frequencies are 6 kHz (a, c) and 11 kHz (b, d) . (For interpretation of the references to color in this figure legend, the reader is referred to the web version of this article.)

The analytical predictions of the directly radiated acoustic pressure SPL are also plotted in Fig. 8(c) and (d) to assess the evolution from directly radiated field to the total response. From Fig. 8(c) it is observed that the addition of reflection and diffraction does not greatly change the acoustic response for $\beta \in [0^{\circ}, 60^{\circ}]$ in all azimuth planes. Compared with the wavelength of 6 kHz, the folding-induced reconfiguration of the Miura-ori array in the x-y plane does not cause phase deviations that greatly alter the far field interference effects around broadside. Therefore the direct radiation is still dominant in these regions. With the increase of the elevation angle in Fig. 8(c), it is seen that the discrepancies between BEM and direct radiation become larger, e.g. the directly radiated SPL is about 20 dB lower than BEM for $\phi = 60^{\circ}$ and 90° . The reason for the increase of deviation is that the contributions of diffraction are more significant than direct radiation in the endfire regions $\beta = 90^{\circ}$, which also occurs in Fig. 6 for the transducer element. It is seen that total acoustic pressure predictions at endfire locations agree more closely with BEM by accounting for diffraction. On the other hand, the predictions of total acoustic response do not perfectly reconstruct the BEM outcomes for $\phi = 0^{\circ}$ and 30° . This is because the non-dimensional ratio of physical dimensions to acoustic wavelength, $k(|\mathbf{r}_{iq}| + |\mathbf{r}_{q}|)$ in Eq. (10), may not be sufficiently large enough for the full accuracy of the diffraction model [27].

In fact, such disagreements are reduced significantly in Fig. 8(d) with the frequency increased to 11 kHz. Taking the most directive azimuth plane of $\phi = 0^{\circ}$ for instance, most the SPL nodes are predicted accurately by the analysis of the total acoustic pressure response. Moreover, it is seen that the directly radiated broadside SPL is evidently lower than the BEM results, while the total response captures the value quantitatively. This phenomenon reveals that under 11 kHz, the reflection contributes more to this location than direct radiation.

To articulate how the reconfigurations of Miura-ori array govern the contributions of reflection and diffraction to the total acoustic field, the SPL values due to distinct wave components are respectively presented in Fig. 9 as the folding angle θ changes. This array is the same with that used in Fig. 8. The receiving location is broadside in Fig. 9(a) where all the oscillating sub-facets directly radiate waves. Fig. 9(b) shows the SPL contributions at an endfire location $(\beta, \phi) = [90^{\circ}, 60^{\circ}]$ for which many discretized sub-facets do not have direct path once the array is folded. For both plots, the driving frequency is 12 kHz and the radial distance is 5 m. Here the largest dimension of the discretized sub-facet remains 3.75 mm, so that at 12 kHz there are still more than 6 sub-facets per acoustic wavelength to ensure model fidelity.

The directly radiated SPL at broadside in Fig. 9(a) is greatly influenced by change in folding angle. A minimum SPL value is found near $\theta=38^{\circ}$. Such fluctuation of SPL is because the reconfigurations of the oscillating facets change the wave interference effects at broadside. It is seen that the maximum SPL of direct radiation occurs for unfolded state, which reveals that folding reduces constructive interference phenomena at broadside. The SPL due to reflection in Fig. 9(a) monotonically increases with the increase of folding angle. This trend is intuitive given that the reflections are enhanced by the increased folding extent and the broadside location is always subjected to reflected fields. For folding extents $\theta \in [36^{\circ}, 44^{\circ}]$, the contributions due to reflections are even greater than direct radiation. Compared with direct radiation

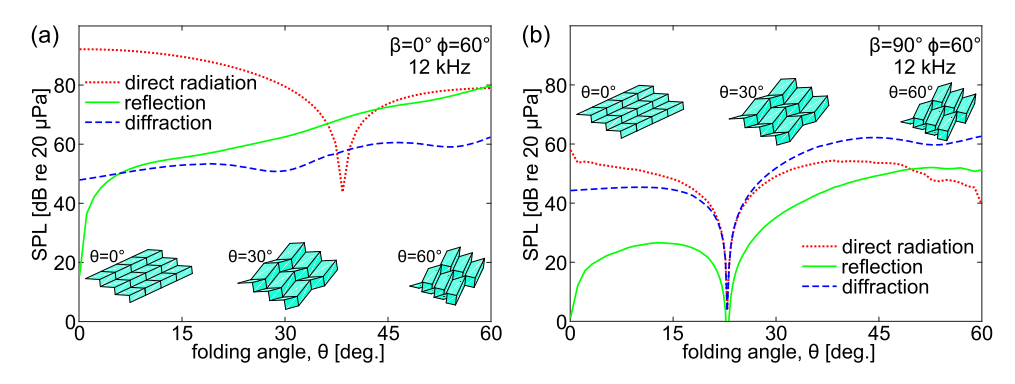


Fig. 9. Analytical predictions of SPL of Miura-ori array (3 \times 2) as a function of folding angle θ . Each plot includes the results for direct radiation, reflection, and diffraction. The locations of the filed points are broadside and (β , ϕ) = [90°, 60°] in (a) and (b), respectively. The driving frequency is 12 kHz.

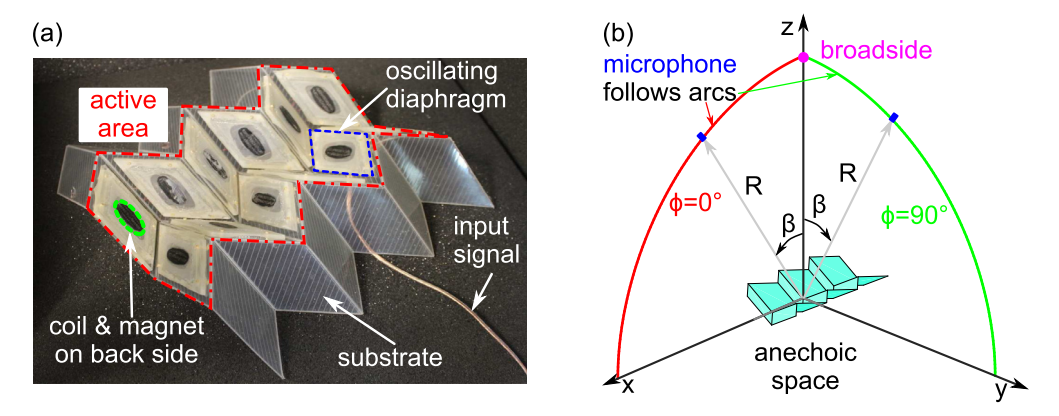


Fig. 10. (a) Experimental specimen of Miura-ori array, in which 3 × 1 Miura-ori elements are equipped with loudspeakers for acoustic radiation. (b) Schematic of experimental setup to measure SPL as the function of elevation angle β at azimuth planes of $φ = 0^\circ$ and 90° .

and reflection, the SPL of diffracted waves is not dramatically influenced by folding. Since the computation of diffraction begins for $\theta=1^\circ$ due to a singularity in the mathematics for $\theta=0^\circ$, the contribution of diffraction is around 48 dB for the nearly flat state of the array with $\theta=1^\circ$. Overall the contribution of diffraction is much smaller than the summation of direct radiation and reflection at broadside.

Yet, for the endfire position $(\beta, \phi) = [90^\circ, 60^\circ]$ in Fig. 9(b), the significance of these wave phenomena is greatly changed. A local minimum occurs around $\theta = 23^\circ$ for all the components since a node of acoustic pressure exists at $(\beta, \phi) = [90^\circ, 60^\circ]$ for this array configuration. For $\theta \in [0^\circ, 23^\circ]$, the waves directly radiated from the array are still predominant. Nevertheless, diffraction becomes the most influential factor in the total acoustic pressure response for greater folding angles since a large proportion of oscillating facets lose the line-of-sight to the endfire location and the reflected waves may also not have a direct path to the field point. These assessments reveal that diffraction is negligible and reflection is prominent for the total response at broadside, whereas the roles reverse for field points at the endfire positions of the reconfigurable tessellated arrays.

4. Experimental validation for analytical framework

To further confirm the efficacy of the analytical model for Miura-ori array, an experimental specimen shown in Fig. 10(a) is fabricated and tested. The array size of the activated part of the specimen is 3×1 , and the facet dimensions are a=56 mm, b=42 mm, and $\gamma=55^\circ$. The origami substrate is made of polypropylene sheet, and the crease pattern is scored on both sides of the plastic by laser cutter (Full Spectrum Laser H-20 \times 12). This process tapers the polypropylene through the thickness to achieve kinematic folding [41]. Miniature electromagnetic loudspeakers are taken apart and reassembled as laminated layers over the origami substrate. The lamination process eliminates the influences of the structural mode of the substrate on the acoustic wave radiation so that the substrate surfaces oscillate in a piston mode. The substrate and lamination process also help to establish an inherent acoustic baffle by preventing acoustic wave radiation from the rear of the experimental specimen. During experiments, to further reduce potential from rearward propagating waves, the specimen is placed on a fiberglass batting surface.

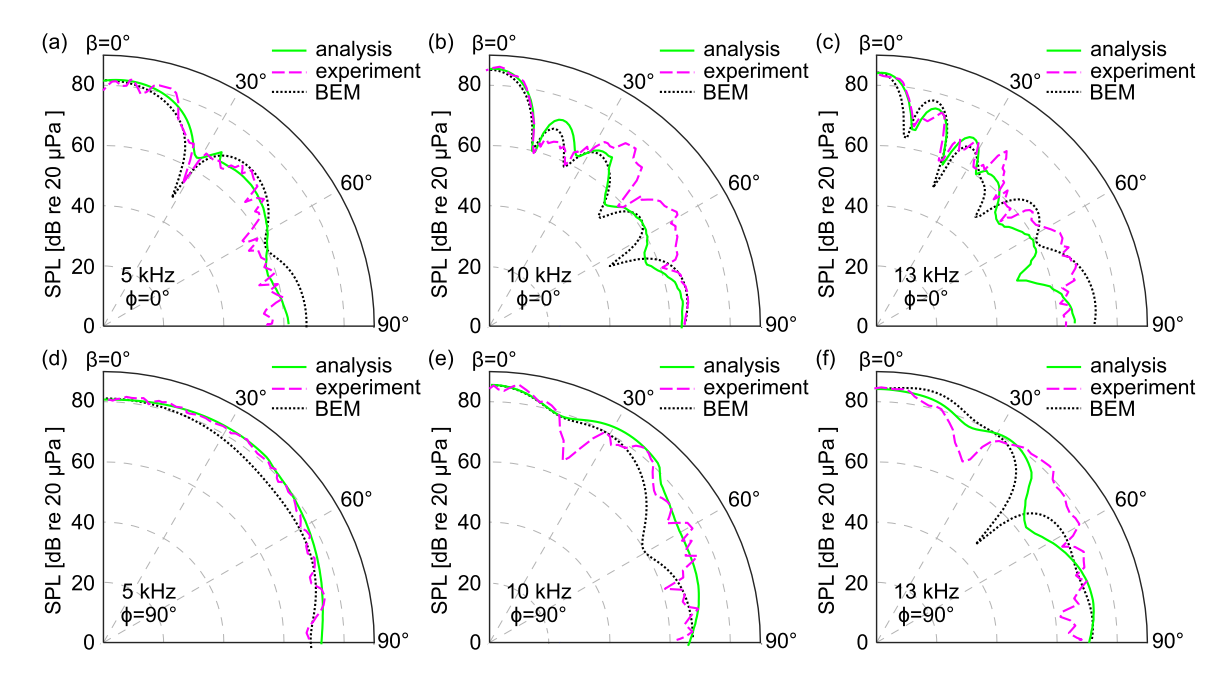


Fig. 11. SPL of Miura-ori array (3 \times 1) as a function of elevation angle β of field point. Each plot compares analytical, experimental, and BEM results. Top and bottom rows correspond to azimuth planes of $\phi = 0^{\circ}$ and 90°, respectively. Folding angle is 60° for all the plots, and driving frequencies are 5 kHz (a, d), 10 kHz (b, e), and 13 kHz (c, f)

The measurements are undertaken in a hemi-anechoic acoustic chamber with usable interior dimensions of 7.8 m by 10.9 m by 4.7 m. As shown in Fig. 10(b), the acoustic pressure is measured by a microphone (PCB Piezotronics 130E20) that follows an arc of constant radial distance $R\approx 2$ m. The radial distance satisfies far field conditions for the cases studied here [42]. The elevation angle β is recorded by a rotary encoder (Signwise) in the range of [0°, 90°]. The data are measured in the azimuth planes of $\phi=0^\circ$ and 90°, respectively. The excitation signal is harmonic and is amplified by an audio amplifier (Pyle PFA300) to drive the loudspeakers on the tessellated substrate. Data are acquired by National Instruments device (NI 6341) and sent to MATLAB for post-processing.

Analytical predictions of SPL are compared with the experimental results in each plot of Fig. 11 along with the BEM outcomes. To capture the influences of reflection and diffraction, the specimen is tested in a highly folded configuration with $\theta=60^\circ$. The top and bottom rows correspond to azimuthal measurements at $\phi=0^\circ$ and 90° , respectively. The driving frequencies are 5 kHz, 10 kHz, and 13 kHz for left, middle, and right columns, respectively.

Considering 5 kHz and $\phi=0^\circ$ in Fig. 11(a), it is seen that the predicted broadside SPL of 82 dB is captured quantitatively well in experiments. With the increase of elevation angle from broadside, two SPL nodes appear around $\beta=30^\circ$ and 60° , and this is observed in both analysis and experiments. In addition, the depths of the measured nodes achieve quantitative agreement with the analytical predictions. When the frequency is doubled to 10 kHz in Fig. 11(b), the response becomes more directive, and four nodes are predicted in analysis. All the SPL nodes are uncovered in measurements with comparable angular locations, despite deviations in magnitude. With further increase of frequency to 13 kHz in Fig. 11(c), reasonable agreements are also observed on the number and location of SPL nodes.

For the azimuthal location of $\phi=90^\circ$ with results shown in the bottom row of Fig. 11, overall the acoustic response is less directive than when the field point is in the azimuthal plane $\phi=0^\circ$. This is due to the fact that the dimension of the radiating area in the y axis ($\phi=90^\circ$) is smaller than that in the x axis ($\phi=0^\circ$) as shown in Fig. 10(b). Therefore less interference effects occur at $\phi=90^\circ$. For 5 kHz in Fig. 11(d), both predicted and measured responses are mostly omnidirectional and the magnitudes of the SPL agree well for all elevation angles. For higher frequencies in Fig. 11(e) and (f), the experiments qualitatively reconstruct the predicted responses with discrepancies that are due to challenges in fabrication accuracy associated with the lamination process that first requires disassembly of the miniature loudspeakers before lamination. These experimental efforts deliver practical support to the significance of diffraction and reflection contributing to the total acoustic pressure emitted from the Miura-ori acoustic array that is revealed by way of the analytical framework created here.

5. Conclusions

This work illuminates the influences of reflected and diffracted waves on the acoustic fields radiated from a reconfigurable tessellated acoustic array. The analytical framework devised here sheds light on these attributes for the first

time, and enriches the understanding of how array reconfiguration alters the interference behaviors induced at far field receiving locations. The findings indicate that reflections are pivotal toward the total acoustic field at broadside of the arrays whereas diffracted waves are the dominant contributor to the acoustic pressure when the receiving location is at endfire locations. The strategies developed here to account for the direct, reflected, and diffracted wave radiation from the Miura-ori tessellation can be extended to arbitrary tessellated radiating architectures. Considering the analogy between acoustics and other wave physics, this work may give guidance for other researchers for whom wave radiation from reconfigurable structural surfaces is of interest [5,7].

Acknowledgment

This work is supported by the National Science Foundation Faculty Early Career Development Award (No. 1749699).

Appendix A

The spatial extents of folded Miura-ori element can be expressed by edge lengths a and b, edge angle γ , and folding angle θ . The mathematic expressions are obtained in Ref. [32] and provided here for sake of being self-contained.

$$H = a \cdot \sin \theta \cdot \sin \gamma \tag{A.1}$$

$$S = b \cdot \frac{\cos \theta \cdot \tan \gamma}{\sqrt{1 + \cos^2 \theta \tan^2 \gamma}} \tag{A.2}$$

$$L = a \cdot \sqrt{1 - \sin^2 \theta \sin^2 \gamma} \tag{A.3}$$

$$V = b \cdot \frac{1}{\sqrt{1 + \cos^2 \theta \tan^2 \gamma}} \tag{A.4}$$

Appendix B

The expression of the barrier plane that facet 1 lies in is

$$\mathbf{N}_{barr}\left(x\mathbf{i} + y\mathbf{i} + z\mathbf{k}\right) = C \tag{B.1}$$

where \mathbf{N}_{barr} is the normal vector of the barrier and C is a constant. As shown in Fig. 1(b), the origin is in this plane, therefore C=0.

The intersection of \mathbf{r}_i and the barrier plane is expressed by

$$(x_{\text{int1}}, y_{\text{int1}}, z_{\text{int1}}) = (x_i, y_i, z_i) + g\mathbf{r}_i$$
 (B.2)

where (x_i, y_i, z_i) are the coordinates of the center of the *i*th source and g is an unknown constant.

Since the intersection is also on the plane, substituting Eq. (B.2) into Eq. (B.1) gives a solution for the constant g.

$$g = -\frac{\mathbf{N}_{barr} \cdot (x_i, y_i, z_i)}{\mathbf{N}_{barr} \cdot \mathbf{r}_i}$$
(B.3)

Then the location of the intersection is

$$(x_{\text{int1}}, y_{\text{int1}}, z_{\text{int1}}) = (x_i, y_i, z_i) - \frac{\mathbf{N}_{barr} \cdot (x_i, y_i, z_i)}{\mathbf{N}_{barr} \cdot \mathbf{r}_i} \mathbf{r}_i$$
(B.4)

Using similar vector method, the intersection of \mathbf{r}_{il} and the y-z plane is found to be

$$(x_{\text{int2}}, y_{\text{int2}}, z_{\text{int2}}) = (x_i, y_i, z_i) - \frac{\mathbf{N}_{y-z} \cdot (x_i, y_i, z_i)}{\mathbf{N}_{y-z} \cdot \mathbf{r}_{il}} \mathbf{r}_{il}$$
(B.5)

where \mathbf{N}_{v-z} is the normal vector of the y-z plane.

Appendix C. Supplementary data

Supplementary material to support the technical investigations on the reflected and diffracted wave fields from the transducer element can be found online at http://dx.doi.org/10.1016/j.wavemoti.2019.03.001.

References

- [1] S. Babaee, J.T.B. Overvelde, E.R. Chen, V. Tournat, K. Bertoldi, Reconfigurable origami-inspired acoustic waveguides, Sci. Adv. 2 (2016) e1601019.
- [2] M. Thota, S. Li, K.W. Wang, Lattice reconfiguration and phononic band-gap adaptation via origami folding, Phys. Rev. B 95 (2017) 064307.
- [3] A. Nanda, M.A. Karami, Tunable bandgaps in a deployable metamaterial, J. Sound Vib. 424 (2018) 120-136.
- [4] K. Fuchi, J. Tang, B. Crowgey, A.R. Diaz, E.J. Rothwell, R.O. Ouedraogo, Origami tunable frequency selective surfaces, IEEE Antennas Wirel. Propag. Lett. 11 (2012) 473–475.
- [5] X. Liu, S. Yao, B.S. Cook, M.M. Tentzeris, S.V. Georgakopoulos, An origami reconfigurable axial-mode bifilar helical antenna, IEEE Trans. Antennas and Propagation 63 (2015) 5897–5903.
- [6] G.J. Hayes, Y. Liu, J. Genzer, G. Lazzi, M.D. Dickey, Self-folding origami microstrip antennas, IEEE Trans. Antennas and Propagation 62 (2014) 5416–5419.
- [7] S. Alharbi, S. Chaudhari, A. Inshaar, H. Shah, C. Zou, R.L. Harne, A. Kiourti, E-textile origami dipole antennas with graded embroidery for adaptive rf performance, IEEE Antennas Wirel. Propag. Lett. 17 (2018) 2218–2222.
- [8] K. Zhang, Y.H. Jung, S. Mikael, J.H. Seo, M. Kim, H. Mi, H. Zhou, Z. Xia, W. Zhou, S. Gong, Z. Ma, Origami silicon optoelectronics for hemispherical electronic eye systems, Nature Commun. 8 (2017) 1782.
- [9] T. Wu, S.S. Hamann, A.C. Ceballos, C.E. Chang, O. Solgaard, R.T. Howe, Design and fabrication of silicon-tessellated structures for monocentric imagers, Microsyst. Nanoeng. 2 (2016) 16019.
- [10] G.M. Schuster, W.M. Mellette, J.E. Ford, Folded monocentric imager with deformable mirror focus, Appl. Opt. 56 (2017) 3435-3444.
- [11] R.L. Harne, D.T. Lynd, Origami acoustics: using principles of folding structural acoustics for simple and large focusing of sound energy, Smart Mater. Struct. 25 (2016) 085031.
- [12] C. Zou, D.T. Lynd, R.L. Harne, Acoustic wave guiding by reconfigurable tessellated arrays, Phys. Rev. A 9 (2018) 014009.
- [13] C. Zou, R.L. Harne, Adaptive acoustic energy delivery to near and far fields using foldable, tessellated star transducers, Smart Mater. Struct. 26 (2017) 055021
- [14] C. Zou, R.L. Harne, Piecewise assembled acoustic arrays based on reconfigurable tessellated structures, J. Acoust. Soc. Am. 144 (2018) 2324–2333.
- [15] I.F. Akyildiz, D. Pompili, T. Melodia, Underwater acoustic sensor networks: research challenges, Ad Hoc Netw. 3 (2005) 257–279.
- [16] F.A. Jolesz, K.H. Hynynen, MRI-guided Focused Ultrasound Surgery, CRC Press, New York, 2007.
- [17] L. Azar, Y. Shi, S.C. Wooh, Beam focusing behavior of linear phased arrays, NDT & E Int. 33 (2000) 189-198.
- [18] L.E. Kinsler, A.R. Frey, A.B. Coppens, J.V. Sanders, Fundamentals of Acoustics, John Wiley and Sons, New York, 2000.
- [19] L. Savioja, U.P. Svensson, Overview of geometrical room acoustic modeling techniques, J. Acoust. Soc. Am. 138 (2015) 708-730.
- [20] U. Ingard. On the reflection of a spherical sound wave from an infinite plane, J. Acoust. Soc. Am. 23 (1951) 329–335.
- [21] A. Krokstad, S. Strom, S. Sørsdal, Calculating the acoustical room response by the use of a ray tracing technique, J. Sound Vib. 8 (1968) 118-125.
- [22] T. Funkhouser, N. Tsingos, I. Carlbom, G. Elko, M. Sondhi, J.E. West, G. Pingali, P. Min, A. Ngan, A beam tracing method for interactive architectural acoustics, J. Acoust. Soc. Am. 115 (2004) 739–756.
- [23] J.F. Allard, G. Jansens, W. Lauriks, Reflection of spherical waves by non-locally reacting porous media, Wave Motion 36 (2002) 143-155.
- [24] L.G. Chambers, The total reflection of a sound pulse of arbitrary form, Wave Motion 2 (1980) 247-253.
- [25] K.M. Li, H.Y. Wong, A review of commonly used analytical and empirical formulae for predicting sound diffracted by a thin screen, Appl. Acoust. 66 (2005) 45–76.
- [26] W.C. Elmore, M.A. Heald, Physics of Waves, McGraw-Hill, New York, 1969.
- [27] W.J. Hadden Jr, A.D. Pierce, Sound diffraction around screens and wedges for arbitrary point source locations, J. Acoust. Soc. Am. 69 (1981) 1266–1276.
- [28] A.D. Pierce, Diffraction of sound around corners and over wide barriers, J. Acoust. Soc. Am. 55 (1974) 941-955.
- [29] A.K. Gautesen, Diffraction of plane waves by a wedge with impedance boundary conditions, Wave Motion 41 (2005) 239-246.
- [30] C.A. Moran, N.R. Biggs, P.G. Chamberlain, Embedding formulae for wave diffraction by a circular arc, Wave Motion 67 (2016) 32-46.
- [31] P.P. Pratapa, P. Suryanarayana, G.H. Paulino, Bloch wave framework for structures with nonlocal interactions: application to the design of origami acoustic metamaterials, J. Mech. Phys. Solids 118 (2018) 115–132.
- [32] M. Schenk, S.D. Guest, Geometry of miura-folded metamaterials, Proc. Natl. Acad. Sci. 110 (2013) 3276–3281.
- [33] K.B. Ocheltree, L.A. Frizzell, Sound field calculation for rectangular sources, IEEE Trans. Ultrason. Ferroelectr. Freq. Control 36 (1989) 242-248.
- [34] S.A. Hambric, S.H. Sung, D.J. Nefske, Engineering Vibroacoustic Analysis: Methods and Applications, Wiley, Chichester, 2016.
- [35] F. Fahy, P. Gardonio, Sound and Structural Vibration: Radiation, Transmission and Response, Academic Press, Oxford, 1987.
- [36] Y.W. Lam, S.C. Roberts, A simple method for accurate prediction of finite barrier insertion loss, J. Acoust. Soc. Am. 93 (1993) 1445-1452.
- [37] Y. Liu, Fast Multipole Boundary Element Method: Theory and Applications in Engineering, Cambridge University Press, New York, 2009.
- [38] V.C. Henriquez, P.M. Juhl, OpenBEM an open source boundary element method software in acoustics, in: Proceedings of Internoise 2010, Lison, Portugal, 2010, pp. 1–10.
- [39] P.M. Juhl, V.C. Henriquez, OpenBEM, Boundary Element Method software, 2015. [Online], www.openbem.dk,
- [40] B.D. Steinberg, Principles of Aperture and Array System Design: Including Random and Adaptive Arrays, Wiley, New York, 1976.
- [41] R.J. Lang, K.A. Tolman, E.B. Crampton, S.P. Magleby, L.L. Howell, A review of thickness-accommodation techniques in origami-inspired engineering, Appl. Mech. Rev. 70 (2018) 010805.
- [42] D.A. Bies, Uses of anechoic and reverberant rooms for the investigation of noise sources, Noise Control Eng. 7 (1976) 154-163.